Mixing of Dense Binary Suspensions: Multi-component Hydrodynamics and Spatial Phase Distribution by PEPT

Antonio Guida, Alvin W. Nienow, and Mostafa Barigou
School of Chemical Engineering, University of Birmingham, Edgbaston, Birmingham, B15 2TT, U.K.

DOI 10.1002/aic.12456
Published online November 17, 2010 in Wiley Online Library (wileyonlinelibrary.com).

The three-component flow field and spatial phase distribution of binary mixtures of glass particles suspended in water in a stirred vessel have been resolved using positron emission particle tracking (PEPT). The Lagrangian flow data provided by the technique have been converted to give a detailed Eulerian description of each of the three phase components of the flow generated by a pitched blade turbine. For the first time, it has been possible to determine the full 3D velocity and concentration fields of the liquid phase and both the solid components within opaque dense slurries of this type containing up to 40 wt % solids. Spatial distributions of local time-averaged slip velocity have also been obtained for each solid component showing wide variations. The detailed PEPT measurements have enabled the solids mass balance and the mass continuity of the three phase components to be accurately verified throughout the vessel. © 2010 American Institute of Chemical Engineers *AIChE J,* 57: 2302–2315, 2011
Keywords: binary suspension, mixing, PEPT, Lagrangian tracking, slip velocity, solid–liquid

Introduction

The processing of solid–liquid suspensions such as bio-slurries, crystallization and catalytic mixtures is frequently conducted in mechanically agitated vessels. In such systems, one crucial aspect is the achievement of good mixing, which allows for an efficient interaction between the different flow components. The methods generally used for designing stirred vessels for solid–liquid mixing tend to be based on a global ''black-box'' approach, and a more detailed description of the internal flow structure has long been missing to enable the development of more rational rules for establishing process parameters and equipment design. The advent of powerful measurement and modeling techniques in recent years has re-energized interest in this field and more effort is increasingly being devoted to try and fully understand the mechanisms behind particle suspension and distribution.[1–4]

Among the various flow visualization techniques, laser Doppler velocimetry (LDV) and particle image velocimetry (PIV) have become the most reliable to examine the complex nature of the flow fields in optically transparent single-phase systems.[5–7] Application to multi-phase studies, however, has been restricted to extremely dilute suspensions as these techniques fail completely in dense systems which are opaque.[1] One of the important aspects in the local description of multi-phase or multi-component mixtures is the measurement of phase distribution, which has remained a challenge. Attempts at local measurements in these systems have been mainly limited to the measurement of mean axial solid-concentration profiles at relatively low concentrations, using a single vertical conductivity or capacitance probe traverse or a withdrawal technique.[8,9] More recent experimental

Correspondence concerning this article should be addressed to M. Barigou at m.barigou@bham.ac.uk.

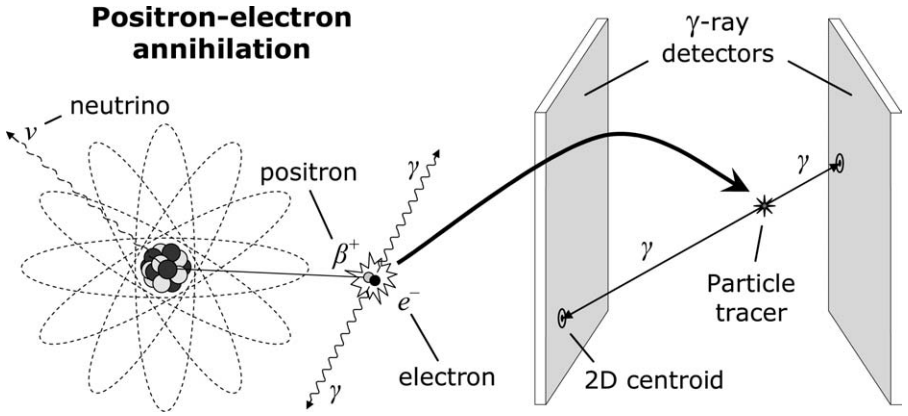

Figure 1. Schematic illustration of positron annihilation and γ-ray detection by the positron camera.

studies using electrical resistance tomography demonstrated, albeit mainly qualitatively, how visualization of gas, solid, or liquid distribution can help improve understanding of mixing processes.[10] However, none of these methods is suitable to probe concentrated suspensions in detail to acquire quantitative information on the local flow dynamics of the different phase components or their individual 3D distribution.

Rammohan et al.[11] developed a more sophisticated computer automated radioactive particle tracking (CARPT) technique based on γ-ray emissions. It has been argued for some time that Lagrangian data obtained from a single particle trajectory, where such data can be accurately determined, may unravel valuable mixing information which is not provided by Eulerian observations.[12–17] The technique of positron emission particle tracking (PEPT) allows noninvasive probing of opaque fluids and within opaque apparatus by using a single small sub-millimeter positron-emitting particle as flow tracer.[14,18] Being able to examine flow phenomena in three dimensions in dense opaque systems that could not be observed as effectively by using other techniques, PEPT is particularly useful for the study of nontransparent multiphase or multi-component flows, where one component can be selectively labeled and its behavior observed.[19,20]

A number of mixing studies have reported that in stirred solid–liquid systems variation in the particle size produces significant effects on the fluid dynamics and phase distribution. For example, Virdung and Rasmuson[21] using LDV measurements showed that the fluid velocity fluctuations due to turbulence in the liquid phase were higher in solid–liquid suspensions than in single phase flow, an effect that increased with particle size. Although their simulations involved particle sizes <0.1 mm, Altway et al.[22] showed that the pattern of solid concentration contours for different particle sizes was qualitatively similar; however, smaller particles showed a more uniform distribution. Using larger particles with 0.1 mm $< d <$ 0.5 mm, Špidla et al.[23] experimentally confirmed by means of a conductivity probe that smaller solid particles generate a more homogeneous suspension. Their results also showed that the homogeneity of the solid–liquid suspension improved with increasing average solid concentration. We recently observed the same effect using coarse monosized glass particles ($d \sim 3$ mm), with more homogeneous suspensions being obtained when the solids content was increased.[24]

In this article, we report on the use of the PEPT technique to study the mixing of dense binary mixtures consisting of glass beads of two different size classes suspended in water. We present for the first time extensive data for these binary systems containing up to 40 wt % solids. Detailed information is obtained on particle and fluid trajectories, which is converted to give a pointwise Eulerian description of the flow field as well as the spatial distribution of each of the liquid and solid components of the mixture.

Materials and Methods

Positron emission particle tracking

The technique of positron emission particle tracking primarily involves the use of a labeled particle tracer, a positron camera and a location algorithm for computing the tracer location. The tracer particle is labeled with a positron-emitting nuclide and the radioisotopes usually used are ^{18}F, ^{61}Cu, and ^{66}Ga. Isotope ^{18}F is the most frequently used and has a half-life of 109 min. It is produced from either purified water or solid materials containing oxygen under direct bombardment with high energy (33 MeV) ^{3}He beams by using a cyclotron. The techniques currently employed for particle labeling are surface modification, direct irradiation, and ion-exchange.[25,26]

A positron emitted by the particle tracer rapidly annihilates with an electron emitting a pair of almost collinear 511 keV γ-quanta in opposite directions. The detection in coincidence of these two γ-rays by the positron camera is the first step in locating the tracer. The positron camera consists of two γ-camera heads working in coincidence and mounted on a motorized gantry, which allows their rotation about a horizontal axis. Each head contains a single sodium iodide crystal optically coupled to an array of photomultiplier tubes.[27] When a positron-electron annihilation occurs the γ-rays emitted produce two coincident scintillations in the crystals, as illustrated in Figure 1, the related photomultipliers generate positional signals and two 2D centroids are calculated by the detection software. The joining line is the photon-trajectory related to the annihilation event. With a small number of

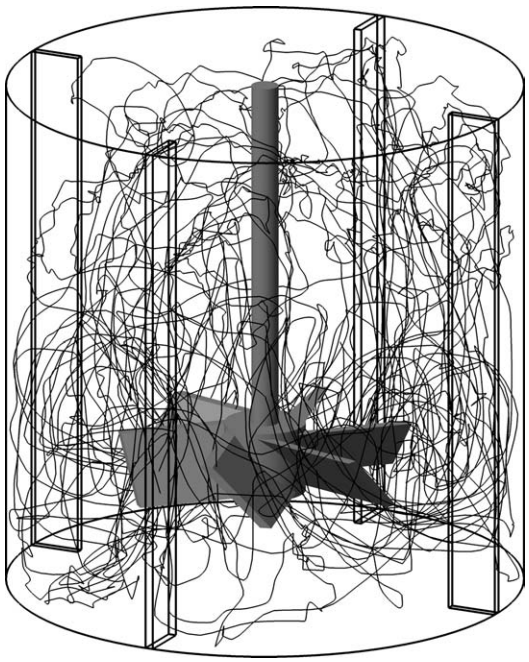

Figure 2. Example of a 3D plot of a neutrally buoyant tracer trajectory in water: Lagrangian tracking time = 1.45 min; Re_{imp} = 40,000.

annihilation events (theoretically only two) the position of a single positron-emitting particle can be located at the intersection of the photon trajectories.

The location algorithm calculates the time-space location of the radioactive tracer minimizing the sum of perpendicular distances from a generic point to the various photon trajectories.[28] Moreover, it discards iteratively the corrupt events caused by Compton scattering, the radioactive background or if the two detected γ-rays were not in fact a pair of 511 keV photons originating from the same positron-electron annihilation event. This Lagrangian tracking approach provides the position of the particle tracer in space at multiple instants, and such experimental data are numerically expressed by four sets of time-space coordinates (t, x, y, z). An example of the 3D plot of a trajectory determined in water in a stirred vessel, based on the 3D visualization of the three space coordinates of a neutrally buoyant tracer is presented in Figure 2.

In the case of a multi-component system, the full 3D trajectory of each component must be resolved separately. Currently, PEPT can most accurately track one particle at a time. For this reason, PEPT multi-component investigations consist of multiple successive and distinct experiments, that is, one for a single-phase system, two for a monodisperse suspension, and three for a binary suspension. These experiments are performed successively, tracking one component at a time in the same unchanged multi-component system.

Experimental apparatus and procedure

The PEPT experiments were conducted in a fully baffled flat-base vessel of diameter $T = 288$ mm, agitated by a 6-blade 45° pitched turbine (PBT) of diameter $D \sim 0.5T$, as

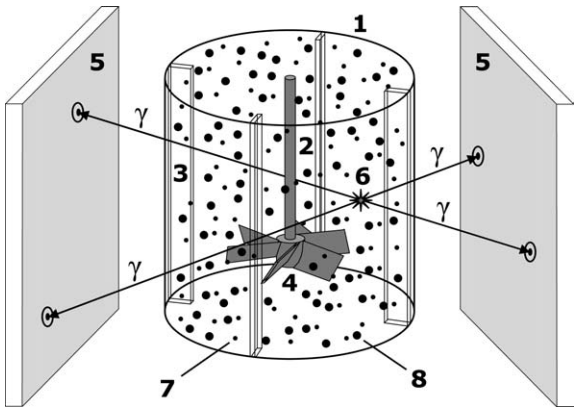

Figure 3. Experimental PEPT set-up for studying the mixing of a binary suspension: 1 tank; 2 shaft; 3 baffle; 4 PBT; 5 γ-ray detectors; 6 PEPT tracer; 7 glass beads ($d \sim 1$ mm); 8 glass beads ($d \sim 3$ mm).

illustrated in Figure 3. The height of the suspension was set at $H = T$ and the impeller off-bottom clearance was $0.25T$. The suspending liquid was an aqueous solution of NaCl of density 1150 kg m^{-3} (NaCl was added to enable the water density to be matched to that of the resin PEPT tracer used to track the liquid) and the solid particles used were spherical glass beads of density 2485 kg m^{-3}. Two nearly monomodal particle size fractions (d_1 = 1.00–1.25 mm, d_2 = 2.85–3.30 mm) were used to make a binary solid–liquid suspension. The two size fractions were mixed in equal proportions with a total solid mass concentration, X, varying from 0 to 40 wt %, that is, $X_1 = X_2 = 0.5X$. Suspension of the solids was investigated with the PBT impeller pumping downward (PBTD). Experiments were conducted at the minimum rotational speed for particle suspension in the binary mixture, N_{js}, visually determined through the transparent walls of the vessel according to the well-known Zwietering criterion[29], that is, no particle should remain stationary on the base of the vessel for longer than 1–2 s. The experimental conditions are summarized in Table 1.

Each component of the suspension was tracked and its full trajectory separately determined in three successive experiments. As pointed out above, although only one component was labeled at a time, both solid components were simultaneously dispersed in the liquid phase in each experiment. A neutrally buoyant radioactive resin tracer of 600 μm diameter was used to track the liquid phase, and from each particle size fraction a representative glass particle was taken, was directly irradiated via a cyclotron and its motion tracked within the agitated slurry. The PEPT tracking time was 30

Table 1. Experimental Conditions

X (wt %)	C (vol %)	N (s^{-1})	u_{tip} (m s^{-1})	Re_{imp}
0	0	5.50	2.49	1.31×10^5
5.0	2.4	6.33	2.87	1.51×10^5
10.0	4.9	7.50	3.39	1.79×10^5
20.0	10.4	8.50	3.85	2.03×10^5
40.0	23.6	10.17	4.60	2.43×10^5

min or higher in each case, long enough so that adequate data resolution was obtained in every region of the vessel and ergodicity of flow, the theoretical condition which guarantees that a flow follower is representative of all the solid or liquid phase it represents, could be safely assumed. In a single phase system, ergodicity or iso-probability condition implies an equal probability of tracer presence at every point in the flow. In a multi-phase system, however, the total probability for all phases is required to be uniform, that is, the sum of the probabilities of presence (weighted by the inverse of the phase volume concentration) of all components of the system must be the same everywhere. Strictly, ergodicity is a theoretical state that can only be approached after an infinite tracking time. However, it can be mathematically shown that, if the probability of tracer visit is sufficiently high everywhere, ergodicity can be safely assumed when the trajectory of the tracer is recorded over a sufficiently long time so that adequate data resolution is achieved in every region.[13] In the flow system examined here, the probability of visit is well-distributed by virtue of the open geometry of the vessel where all regions are more or less equally accessible by the tracer, and the highly turbulent state of the suspension ($Re_{imp} = ND^2/\nu > 10^5$). Confirmation of the ergodicity assumption through experimental verifications has been reported in a previous article.[30]

Data analysis

As described above, PEPT provides the Cartesian (x, y, z) coordinates of a single particle tracer moving within the system being studied as a function of time. A new code was developed to analyze PEPT flow data; it uses cylindrical coordinates to calculate Lagrangian velocities along the trajectory of the tracer using the least squares method locally. These Lagrangian velocities are then converted to Eulerian velocities using a 3D user-defined grid consisting of a large number n_c of equal volume cells. In a given cell, the code determines for each tracer visit the mean cylindrical velocity components (u_ϑ, u_r, u_h) along the segment of trajectory intersecting with the cell, and averages the values again by the number of visits. A number of other local quantities are determined within each cell including the magnitude of the total 3D velocity and of the 2D radial–axial velocity, standard deviation of the velocity components and of the total velocities (2D and 3D), tracer acceleration, number of PEPT tracer locations, cumulative residence time, probability of tracer presence, and frequency of visits.

In addition to location and velocity information, PEPT allows the particle-tracer occupancy distribution within the vessel volume to be computed, which offers an additional powerful tool for characterizing flow behavior within any batch system. Occupancy has traditionally been obtained by calculating the fraction of the total experimental time, t_∞, spent by the tracer in each cell during the experiment. Such a definition establishes a mathematical identity between occupancy and probability of presence of the particle tracer, but undesirably makes occupancy highly dependent on the density of the grid so that as the number of cells increases occupancy tends to zero. If the cells are chosen to have equal volume, however, this problem is circumvented by using the "ergodic time" defined as $t_E = t_\infty/n_c$, instead of the total experimental time t_∞.

The ergodic time represents the time that the tracer would spend in any cell if the flow was single phase and ergodic, an asymptotic status in which the flow tracer has exactly an equal probability of presence everywhere within the system. Thus, the local occupancy, O_j, can be defined as:

$$O_j = \frac{\Delta t_j}{t_E}, \tag{1}$$

where Δt_j is the time that the tracer of the j-th component (solid or liquid) of the mixture spends inside a given cell. For the binary systems examined in this work, the index j assumes values 1, 2, or 3 where $j = 1, 2$ denotes the solid components, and $j = 3$ denotes the liquid phase also sometimes designated by the symbol L.

Given the above definition, the average value of the occupancy is 1 independently of the chosen number of grid-cells n_c. Considering the system at hand, a specific small solid particle having diameter d_j selected from the solid component j has an infinitesimal probability, $f(\mathbf{P})dV$, to be present inside an infinitesimal volume element dV, which is a function of the particle position $\mathbf{P}$ and can be expressed from two different points of view. From the Lagrangian point of view, it is the ratio of the infinitesimal time dt_j that the solid particle spends inside dV to the total time of detection t_∞. In Eulerian terms, however, it is the ratio of the number of solid particles dn_j, contained in dV, to the total number of such particles in the vessel n_j. Consequently, it follows that:

$$\left\{ f(\mathbf{P})dV = \frac{dt_j}{t_\infty} \text{ and } f(\mathbf{P})dV = \frac{dn_j}{n_j} \right\} \Rightarrow \frac{dt_j}{t_\infty} = \frac{dn_j}{n_j}. \tag{2}$$

Considering the j-th solid component, and introducing the volume of a single particle V_{Pj}, the infinitesimal solid volume dV_j in dV, the solid volume present in the tank V_j, the local solid volume concentration c_j, the mean solid volume concentration in the vessel C_j, and the total volume of the multi-phase suspension in the vessel V_T, we obtain:

$$\frac{dn_j}{n_j} = \frac{V_{Pj}dn_j}{V_{Pj}n_j} = \frac{dV_j}{V_j} = \frac{c_j dV}{C_j V_T}. \tag{3}$$

Combining Eqs. 2 and 3 leads to a clear correlation between the time that the tracer spends inside dV and the local solid volume concentration, that is:

$$\frac{dt_j}{t_\infty} = \frac{c_j dV}{C_j V_T}. \tag{4}$$

If the cell volume, ΔV, in the grid is uniform, the total number of grid cells is then $n_c = V_T/\Delta V$, and rewriting the above equation in discrete terms gives:

$$\frac{\Delta t_j}{t_\infty} = \frac{c_j \Delta V}{C_j V_T} \Rightarrow \frac{\Delta t_j}{t_E} = \frac{c_j}{C_j}. \tag{5}$$

Now, using the definition given by Eq. 1 for the occupancy O_j as the ratio of time that the tracer spends inside a cell to the ergodic time, Eq. 5 then finally becomes:

$$O_j = \frac{c_j}{C_j}. \quad (6)$$

Note that while Eq. 6 has been derived for a discrete phase component, it is equally valid for the continuous fluid component ($j = 3$). The consequential implication that readily follows from Eq. 6 is that, in addition to local phase velocity, it is now possible to fully resolve by PEPT the local concentration distribution of each flow component (solid and liquid) in an opaque multi-phase system.

Results and discussion

Extensive data were obtained through Lagrangian tracking of the solid and liquid components of the binary suspensions described above. Results are presented as azimuthally-averaged Eulerian maps or profiles, which represent the whole flow field including the effect of the baffles. This is an effective way of presenting 3D data in a reduced form. Furthermore, to enable efficient consultation and comparison of data, results are presented in a concise format using sets of images judiciously produced by grouping together multiple graphs, grayscale contours, or vector plots. Results include for each component of the mixture, flow fields, spatial distributions, slip velocities, flow numbers, and uniformity indices. Finally, evidence of the reliability of the PEPT technique and the related data analysis is provided via three-component mass continuity calculations conducted throughout the vessel.

Flow fields

Using the code outlined above, PEPT raw data were analyzed by defining a cylindrical grid consisting of $n_c = 512$ equal volume cells. The vector velocity map of the agitated liquid obtained with no solid particles present in the vessel ($X = 0$ wt %) is shown in Figure 4 for an impeller rotational speed $N = 5.5$ s^{-1} = 330 rpm. Using cylindrical coordinates, the radial-axial 2D velocity map was obtained by azimuthally averaging the 3D velocity data and projecting them onto the 2D radial-axial plane (rh). As pointed out above, whilst 2D, these flow maps are representative of the whole 3D velocity field. The observed flow field with a single flow loop is typical of a down-pumping PBT with a low impeller off-bottom clearance. As expected, fluid velocities are relatively high in the impeller region and around the flow loop, but low in the upper parts of the tank and in the center of the loop. For ease of comparison, all the velocity plots presented are normalized by the impeller tip speed, u_{tip}.

The effects of the mean solid concentration, X, on the velocity fields of the liquid phase and the two solid components are depicted in Figure 5. A comparison of the liquid flow maps under single-phase flow conditions (Figure 4) and in the presence of the solid phase (first row in Figure 5) shows global qualitative similarities in the flow pattern even at $X = 40$ wt %. A more detailed scrutiny of the images reveals that, excluding the impeller discharge region, no significant quantitative changes occur in the velocity field up to 20 wt % solids, but a distributed small diminution of the normalized velocity is observed at $X = 40$ wt %. In addition, the contours suggest that the normalized velocity in the discharge region diminishes as X increases up to 10 wt %, but slightly recovers at 20 wt % before further declining at 40 wt %.

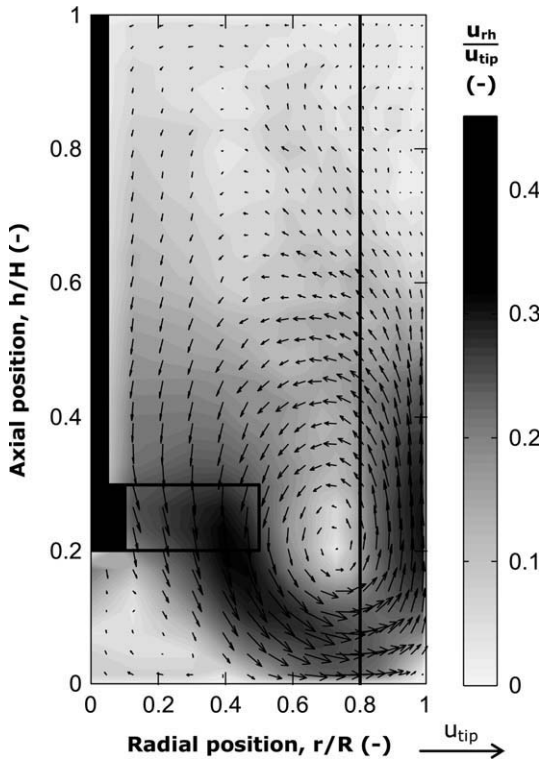

Figure 4. Azimuthally averaged radial–axial velocity map of the liquid phase in the absence of solid particles ($X = 0$ wt %) at $N = 5.5$ s^{-1}.

Unlike the liquid phase, more significant qualitative and quantitative variations in the flow field can be observed for the smaller solid particles having $d \sim 1$ mm, as shown in the second row of Figure 5. At $X = 5$ wt %, the flow field is affected by large fluctuations which make the vector plot appear slightly irregular. This is caused by the scarce presence of solids in the upper part of the vessel, which drops to almost zero close to the surface; such an effect was visually confirmed during the experiments and will be highlighted again below when analyzing the phase distributions. Whilst the normalized velocity in the discharge region decreases monotonically as X increases from 5 wt % to 40 wt %, the center of the loop slowly shifts upwards from $h = 0.2H$ ($X = 5$ wt %) to $h = 0.25H$ ($X = 40$ wt %).

Similarly, the flow fields of the second solid component consisting of glass beads with $d \sim 3$ mm (third row in Figure 5), are affected by the low particle occupancy of the upper part of the tank. In this case, however, the irregularities are more pronounced and extend to the suspension with $X = 10$ wt %. In a similar way to the smaller particles, there is a clear damping of the solid flow field in the impeller region at $X = 40$ wt %.

The above considerations are complemented by Figure 6, which shows the contours of the azimuthally-averaged tangential velocity component for the three components of the suspension. As expected, all the grayscale maps exhibit their maxima (0.2–0.25u_{tip}) near the lower tip of the impeller

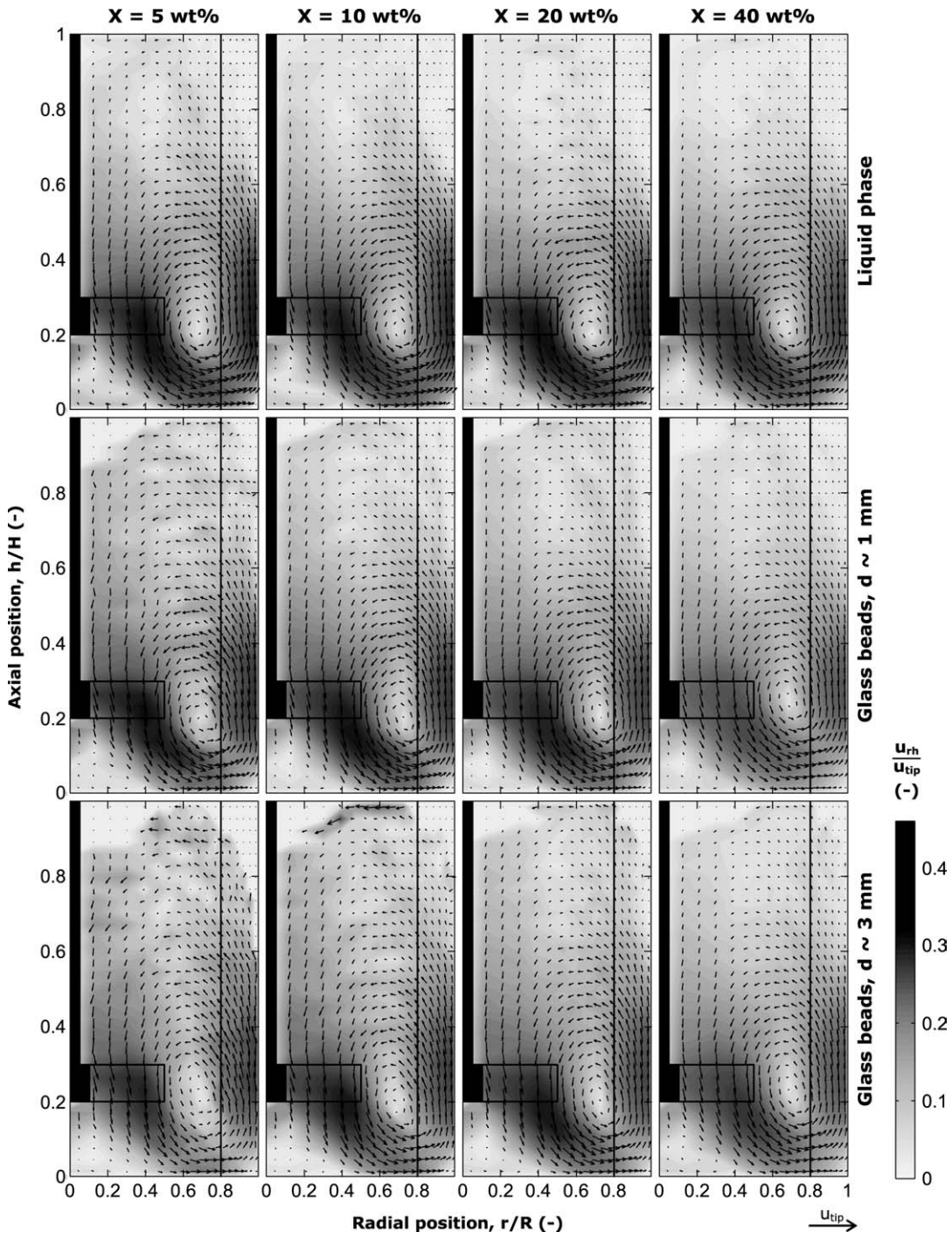

Figure 5. Azimuthally averaged radial–axial velocity maps of the three components of the suspension at varying *X*; *N* = N_{js}.

blades. The liquid phase is characterized by the highest tangential velocities whose magnitude and spatial distribution are not significantly affected by X. In a similar way to the radial-axial velocities, at 5 wt % the contours of the two solid components are affected by small irregularities, which generate a uniformity effect in the velocity map of the larger particles. Both solid components show significantly reduced tangential velocities for $X = 40$ wt %

The observations made above are quantitatively confirmed in Figure 7, which shows details of the effects of the mean solid concentration on the three velocity components for each component of the mixture. The plots exhibit radial distributions of the velocity components (u_ϑ, u_r, u_h) in the horizontal impeller discharge plane, that is, along the lower edge of the impeller blade at $h = 0.2H$. In a similar way to the flow maps discussed above, all the velocity plots have been normalized by the impeller tip

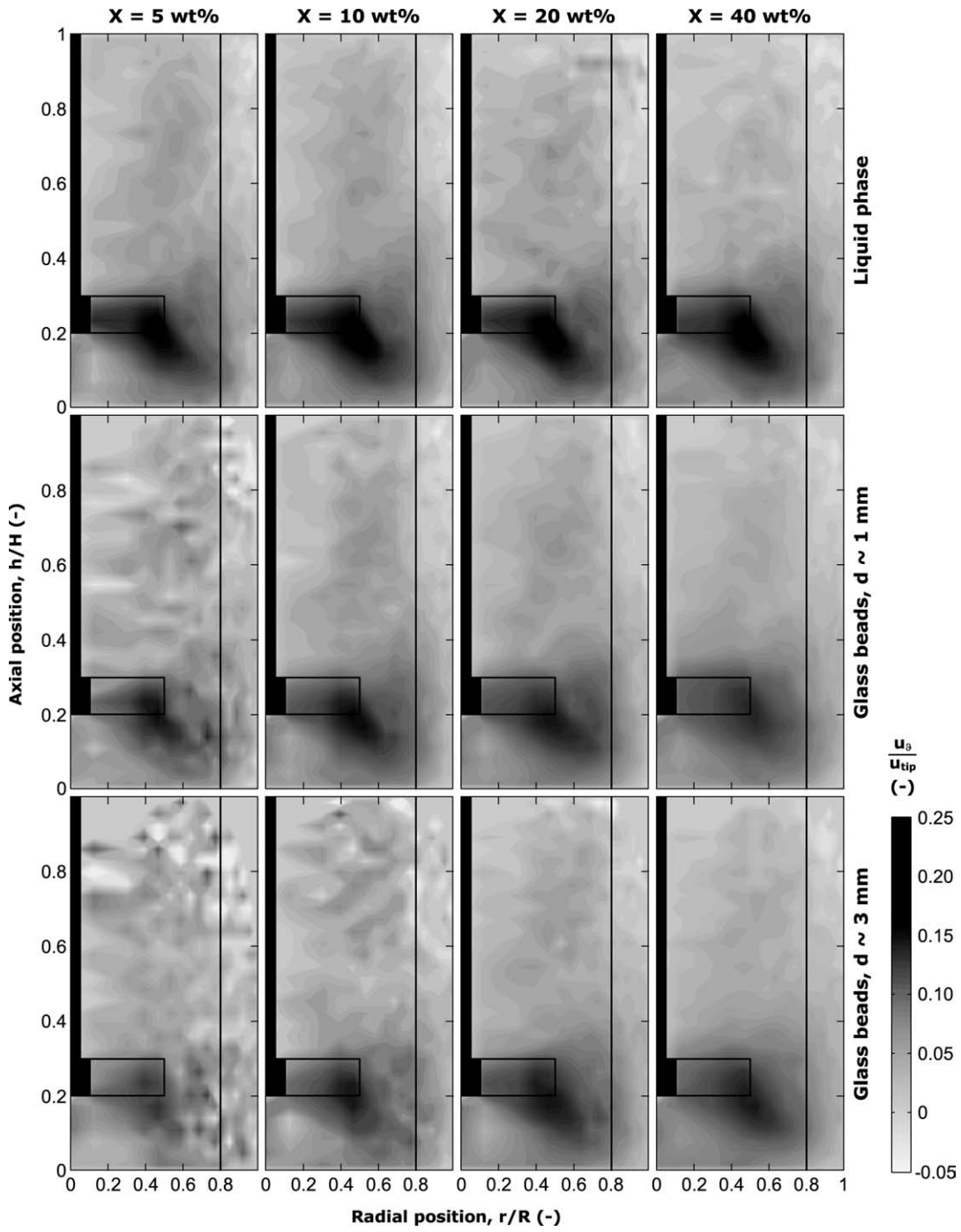

Figure 6. Azimuthally-averaged tangential velocity maps of the three components of the suspension at varying *X*; $N = N_{js}$.

speed, u_{tip}, for ease of comparison. As expected, due to the type of agitator used, the dominant velocity component in this plane for all the mixture components is the axial u_h. The tangential velocity component is only significant close to the impeller and falls off to almost zero away from it. The radial component for all phase components is generally relatively small, except at 40 wt % solids where for both solid components it is comparable to the tangential component.

Time-averaged slip velocity maps

The primary objectives of solid–liquid mixing include creating and maintaining a slurry, and enhancing the rate of mass or heat transfer between the solid and the liquid phase. Heat and mass transfer coefficients are significantly influenced by the relative velocity between phases, also known as slip velocity. Such an important hydrodynamic variable obviously varies from point to point within a stirred vessel

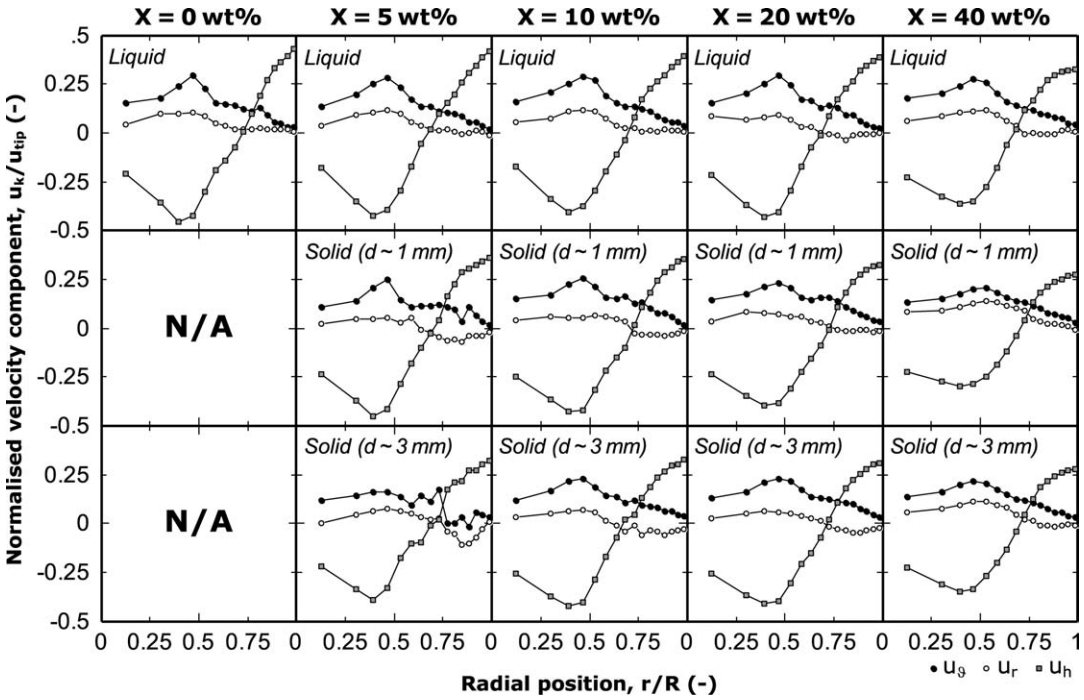

Figure 7. Azimuthally averaged radial profiles of the three velocity components in the horizontal impeller discharge plane at $h = 0.2H$; $N = N_{js}$.

and there are no techniques available for measuring it. Consequently, in practice, the particle settling velocity has often been taken as a guess estimate of the slip velocity.[31]

Neglecting any contribution to slip, which might arise from possible rotation of a particle about its center, the magnitude of the local time-averaged slip velocity vector can be determined for each solid component j, thus:

$$s_j = \sqrt{\left(u_\vartheta^{(L)} - u_\vartheta^{(j)}\right)^2 + \left(u_r^{(L)} - u_r^{(j)}\right)^2 + \left(u_h^{(L)} - u_h^{(j)}\right)^2}. \quad (7)$$

In consequence, the radial-axial and tangential velocity data presented in Figure 5 and 6 can be used to map the local time-averaged slip velocity.

The effects of the mean solid concentration on the spatial distribution of the normalized slip velocity for each solid component of the mixture are shown in Figure 8. The irregularities of the solid flow fields attributed to the scarce presence of solid particles in the upper part of the vessel, as discussed above in relation to Figure 5, cause analogous effects in the slip velocity maps at $X = 5$ wt % for the smaller particles and up to $X = 10$ wt % for the larger particles.

There are wide variations in the spatial distribution of s_j. As a consequence of Eq. 7, which combines radial-axial and tangential contributions, the regions of maximum slip velocity occasionally correspond with the lower tip of the impeller blades (tangential dominance), with the discharge region of the impeller (radial-axial dominance), or with both areas when there is a more balanced contribution of the three cylindrical components of the slip velocity vector. For both particle size fractions, the areas above the impeller and in the upper part of the vessel, that is, $h > 0.4H$, are characterized by a gradual but significant reduction in the slip velocity with increasing X. A similar reduction is observed in the rest of the vessel for particles with $d \sim 3$ mm.

Spatial solid and liquid distribution

On the basis of Eq. 6, in each binary suspension the local occupancy can be obtained for each solid component and the liquid; consequently, the volume concentration of each component can be mapped. The spatial distributions can be effectively compared using purposely created maps, where the radial–axial plane is divided into square boxes containing information for every solid and liquid component, as shown in Figure 9a. Each box contains two shaded bars: the fraction of the box area occupied by each bar is equivalent to the local volume of the corresponding solid component, while the remaining white area is equivalent to the local liquid volume. Furthermore, by using bars of equal base, their height is also proportional to the local solid volume concentration and, thus, horizontal profiles of solid concentration for each solid component can be represented at each horizontal level as depicted in Figure 9b.

The spatial distribution of the volume fraction of both particle size classes is shown in Figure 10 for $X = 5$–40 wt %. As these 2D maps were obtained from azimuthally averaged data, the area of each square cell is representative of the volume of the related 3D cell (a torus with a square cross section). A high solid accumulation underneath the impeller is visible for every value of the mean solid concentration. This effect is more pronounced for larger glass particles, so that the local solid volume concentration of the larger particles ($d \sim 3$ mm) is about twice the concentration of the smaller particles ($d \sim 1$ mm) up to $X = 20$ wt %. At $X = 40$ wt %,

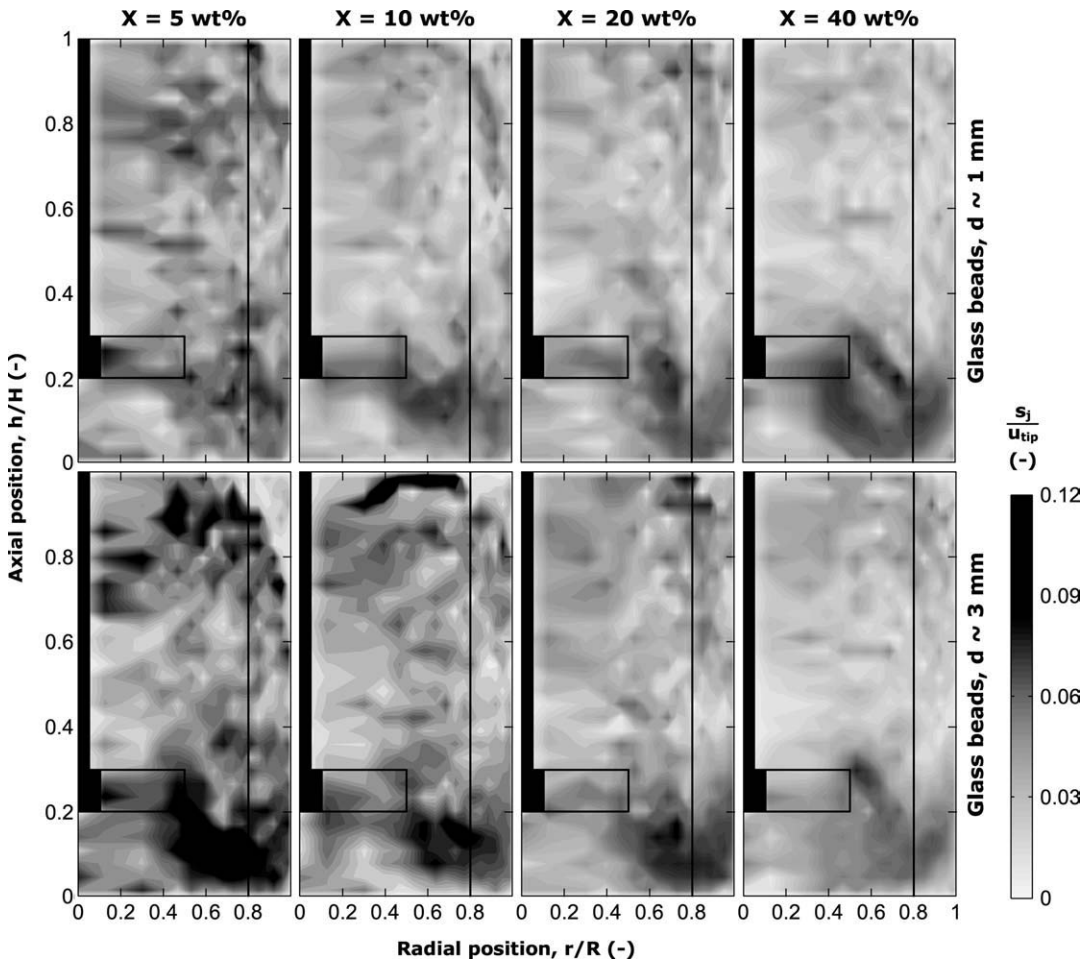

Figure 8. Normalized azimuthally averaged maps of time-averaged slip velocity of the solid components of the suspension at varying X; $N = N_{js}$.

the accumulation underneath the impeller is still high compared to the rest of the tank, but overall the solids distribution appears much more uniform than for lower X values, especially in the case of the smaller particles. This result suggests that at $N = N_{js}$ the accumulation below the turbine reduces for smaller particles and/or higher solids concentrations.

Moreover, information on the radial and vertical average concentration profiles is also provided in Figure 10; whilst to the right of each map the vertical profile of the radially-averaged volume concentration is shown, the radial profile of the vertically averaged volume concentration is shown above the map. The average radial profiles are more or less flat for both particle size fractions, whereas the vertical profiles show similar behavior at every X value. To compare such vertical profiles, normalized values of the azimuthally and radially averaged volume concentration, c_h, of each particle size class are plotted in Figure 11. The plots highlight the nonuniformity of the solids distribution, with a minimum at the impeller plane and a maximum above it, near the central plane. The proximity of the profiles to the vertical line $c_h/C_j = 1$ for smaller particles and/or higher solids concentrations, corrobates the point previously highlighted that local solids build up diminishes under these conditions.

The shape of the curves in Figure 11 bears a good resemblance to the so-called "belly-plots" reported in the literature in a number of studies using either a single vertical probe traverse or a withdrawal technique.[9] The PEPT results presented here, however, are much more detailed as local solid concentration values are accurately determined on a pointwise 3D grid covering the whole vessel, which has not been possible before with any technique including sampling and probe methods. Furthermore, other techniques cannot distinguish between different particle size classes in the same suspension.

Global indices for multi-phase mixing

Flow number. To further assess the magnitude of the effect of the presence of particles on the flow field inside the stirred vessel, the dimensionless flow number was estimated. Because of the considerable quantity of solids used, the volumetric flowrate discharged by the agitator needs to be determined separately for each phase component taking into

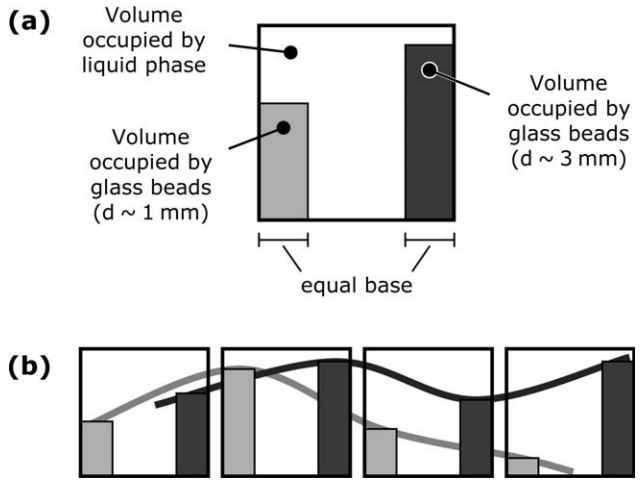

Figure 9. Representation of the local concentration of the three suspension components: (a) square box containing information for every solid and liquid component; (b) a sequence of adjacent boxes depicting two horizontal solid volume concentration profiles.

account its local volume concentration. For each component of the mixture, $Q^{(j)}$ was calculated along the horizontal lower edge of the impeller blade corresponding to the impeller discharge plane, by integrating the axial velocity profile weighted by the local volume concentration, that is, by c_1 and c_2 for the solid components and by c_3 for the liquid phase. Thus, the usual definition of the flow number used to estimate the pumping effectiveness of impellers in single-phase systems was extended to this two-phase three-component problem. The flow number was computed for each component using the following expression:

$$Fl^{(j)} = \frac{Q^{(j)}}{ND^3} = \frac{1}{ND^3} \int_{PBT} c_j u_h^{(j)} dS, \tag{8}$$

where the integral is evaluated over the horizontal discharge edge of the impeller blade ($h = 0.2H$ and $r \leq 0.5R$). The sum of $Q^{(L)}$, $Q^{(1)}$, and $Q^{(2)}$ represents the total volumetric discharge, Q, and introducing the total two-phase flow number, Fl, it follows that:

$$Fl = \frac{Q}{ND^3} = \frac{Q^{(L)} + Q^{(1)} + Q^{(2)}}{ND^3} = Fl^{(L)} + Fl^{(1)} + Fl^{(2)}. \tag{9}$$

As shown in Figure 12, low to moderate solid concentrations up to 10 wt % seem to cause a small reduction in $Fl^{(L)}$, which is not compensated for by the simultaneous increase in $Fl^{(1)}$ and $Fl^{(2)}$ (mainly due to the local rise in c_1 and c_2); thus, the total flow number, Fl, diminishes from 0.86 to 0.77. At higher solid concentrations above 20 wt %, the approximately linear increase in $Fl^{(1)}$ and $Fl^{(2)}$ fails to counterbalance the steep reduction in $Fl^{(L)}$ caused by the presence of solid particles, consequently leading to a substantial fall in Fl. Overall, Fl incurs a reduction of ~20% when X rises from 0 to 40 wt %.

Average slip velocity. The qualitative observations noted above, in relation to Figure 8, concerning the reduction in slip velocity with an increase in mean solid mass concentration, can be effectively quantified by evaluating an average of the azimuthally-averaged values of normalized slip velocity across the whole radial-axial plane. Using a grid, with equal volume cells, guarantees that the arithmetic mean of slip velocity coincides with the volume-weighted average. These space-averaged slip velocity values are normalized

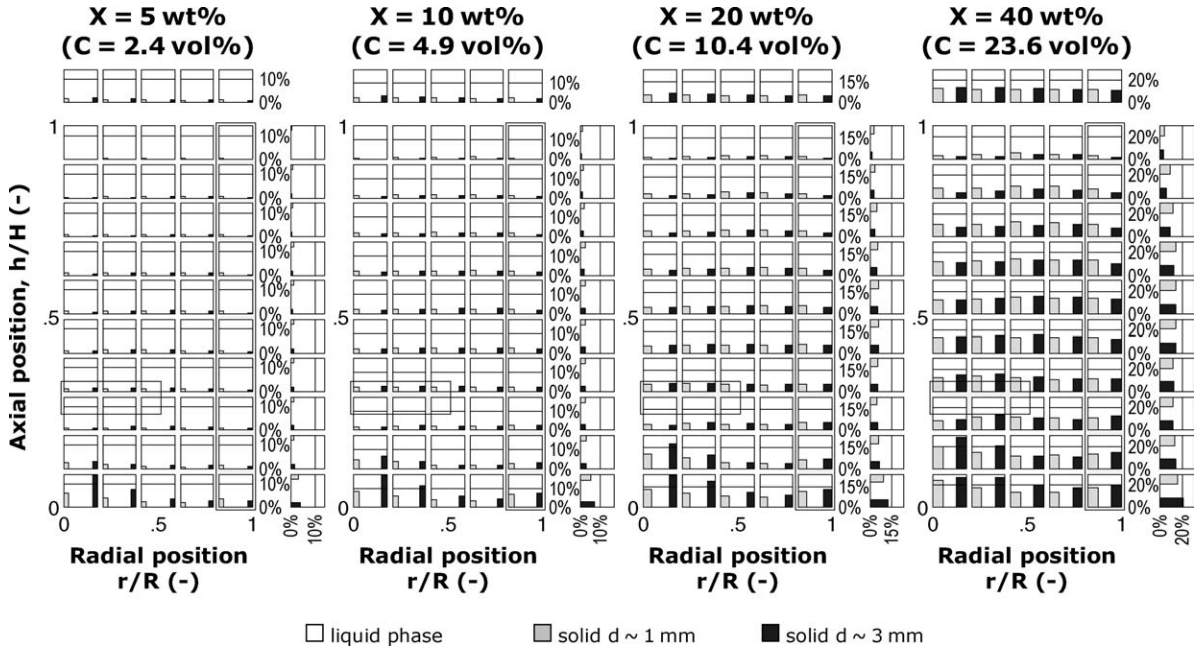

Figure 10. Azimuthally-averaged local volume concentration maps for the three components of the suspension at varying *X*. Note that unless otherwise specified the symbol "%" indicates "vol %."

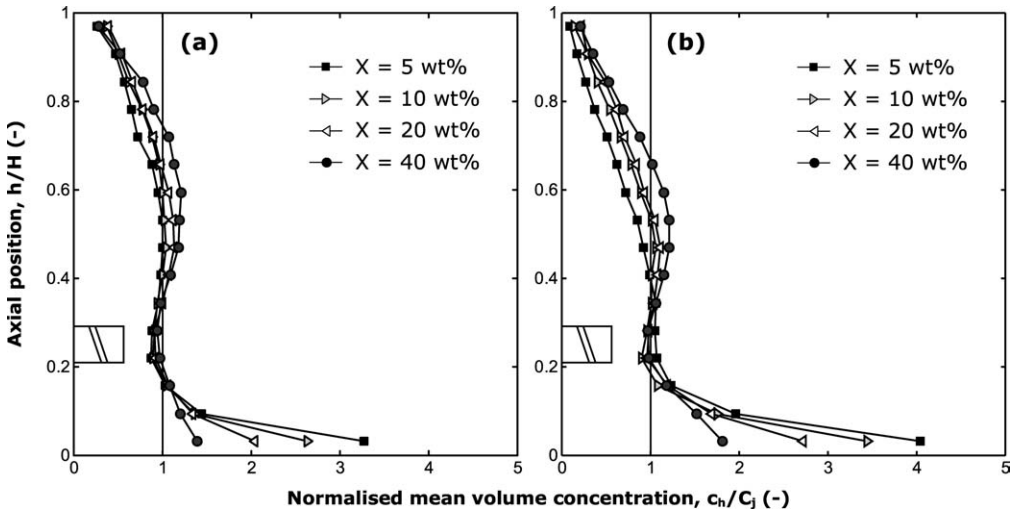

Figure 11. Vertical normalized profiles of azimuthally and radially-averaged solid volume concentration at $N = N_{js}$: (a) ~1 mm glass beads; (b) ~3 mm glass beads.

and plotted as a function of X in Figure 13 for both particle size fractions. As expected, for both solid components the normalized average slip velocity, $\overline{s}_j/u_{tip}$, decreases with X. Starting at $X = 5$ wt % with a value of $\overline{s}_2$ 37% higher than $\overline{s}_1$, both $\overline{s}_j/u_{tip}$ values rapidly fall off to a similar value (~0.034) as X increases to 40 wt %. Hence, it can be concluded that at high solid concentrations the normalized average slip velocity is considerably reduced, but it is not entirely clear whether it loses its dependence on particle size.

Uniformity of suspension. The substantial variation of the local solid concentration throughout the vessel, as demonstrated by the maps in Figure 10 and the axial profiles in Figure 11, warrants the use of a further global index to enable a quantitative description of the spatial uniformity of the solids distribution.[24] For each particle size fraction a uniformity index can be defined as:

$$\xi_j = \frac{1}{\sigma_j^2 + 1} = \frac{1}{\frac{1}{n_c}\sum_{i=1}^{n_c}\left(\frac{c_j^{(i)} - C_j}{C_j}\right)^2 + 1} = \frac{C_j^2}{\left\langle c_j^2 \right\rangle}, \qquad (10)$$

where i is the cell number within the measurement grid. The index is conveniently defined so that as $\xi_j \to 0$ the uniformity of the j-th solid component is at its minimum (condition achieved for a theoretically infinite variance, σ_j^2, of the normalized local concentration); and when $\xi_j = 1$ the solids are uniformly distributed within the vessel volume, that is, there are no concentration gradients and the related local concentration everywhere is equal to the average concentration, C_j, in the vessel (i.e., $\sigma_j^2 = 0$). Values of the index ξ_j at varying average mass concentrations are plotted in Figure 14, for both particle sizes, showing that ξ_j increases with X. This seems to suggest, perhaps counter-intuitively, that as long as the particles are in the "just suspended" mode more concentrated suspensions will tend toward a homogeneous state by virtue of their increased solids loading. The smaller particles, however, are significantly better dispersed than the larger ones at all the values of X used here.

Verification of mass balance and mass continuity

The pointwise measurements obtained with PEPT have enabled the solids mass balance throughout the vessel to be accurately verified, that is, the measured local values of the two solid volume concentrations balance the experimental parameter $C_j = V_j/V_T$, so that:

$$\frac{1}{n_c}\sum_{i=1}^{n_c} c_j^{(i)} \equiv C_j. \qquad (11)$$

The identity symbol "$\equiv$" appears in Eq. 11 because the local concentration is obtained from Eq. 6 through the measurement of local values of the occupancy O_j whose average value is by definition identically equal to 1.

Another important tool for checking the accuracy and reliability of flow data is mass continuity. The net mass flux

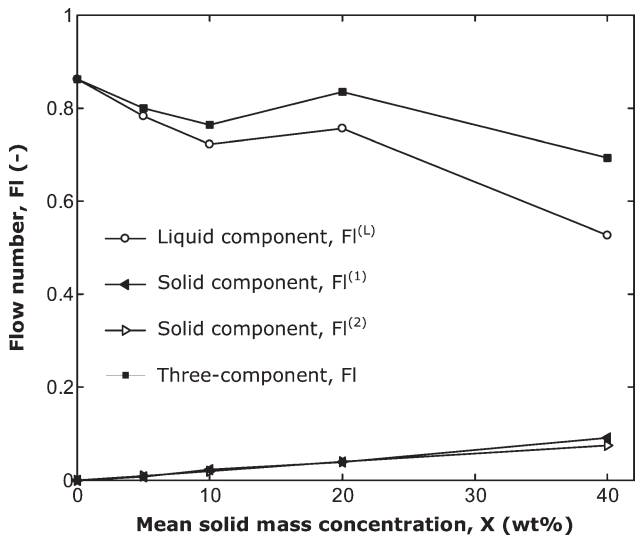

Figure 12. Effect of the mean mass concentration of the solid phase on the flow number.

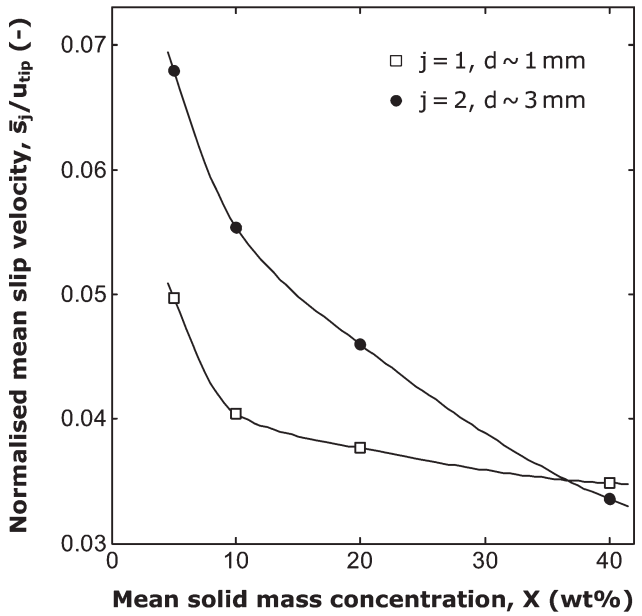

Figure 13. Variation of the normalized mean time-averaged slip velocity as a function of the mean solid mass concentration.

through a volume bounded by a closed surface S should be zero, thus:

$$\sum_S \mathbf{u}^{(j)} \cdot \Delta\mathbf{S} \cong 0. \tag{12}$$

Calculations can be made by considering a closed cylindrical surface S with the same vertical axis, base and diameter as the tank but of a shorter height. Because the vector $\mathbf{u}$ is zero over the external surface of the vessel or is parallel to it, the term $\mathbf{u}\cdot\Delta\mathbf{S}$ is zero everywhere except in the horizontal plane across the tank, so that S can be reduced to such a plane, S_h, and Eq. 12 is reduced to a zero average of axial velocities across the horizontal plane considered. Alternatively, a similar situation can be envisaged where S is a closed cylindrical envelope with the same vertical axis and height as the tank but with a smaller diameter; Eq. 12 then becomes a zero average of radial velocities across the lateral surface, S_r, of the considered cylindrical volume. These two types of surfaces, S_h and S_r, were numerically introduced in the vessel and the continuity test was applied to all the sets of PEPT data collected in this study. The results are summarized in Figure 15, showing a very good verification of the mass continuity as the velocity average across the given surface in each case is close to zero, generally less than $0.03u_{tip}$.

Conclusions

The Lagrangian technique of positron emission particle tracking has been successfully applied to the study of dense solid–liquid binary suspensions. The Lagrangian flow data provided by the technique have been converted to give a detailed Eulerian description of each of the three phase components of the flow generated by a pitched blade turbine. For the first time, it has been possible to determine the full

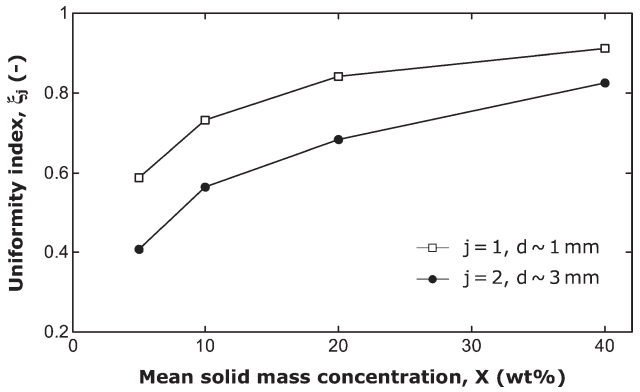

Figure 14. Variation of the uniformity index ξ_j as a function of the mean solid mass concentration.

3D velocity field and spatial distribution of the liquid phase and of each particle size fraction within a binary suspension. In addition, a substantial amount of unique experimental data on local hydrodynamics and homogeneity of suspension have been obtained in solid–liquid flows of such high concentrations, reaching 40 wt %. Such detailed results could be used to inform the design of experiments to study mixing phenomena or equipment design to maximise the global or local mixing efficiency of the system.

The accuracy of the PEPT measurements has been ascertained through multi-component mass continuity verifications throughout the vessel. Values of the multi-component flow number indicate that the pumping effectiveness of the PBT agitator is preserved for low to moderate concentrations. At high solid concentrations, however, the multi-component flow number and normalized mean slip velocity for both

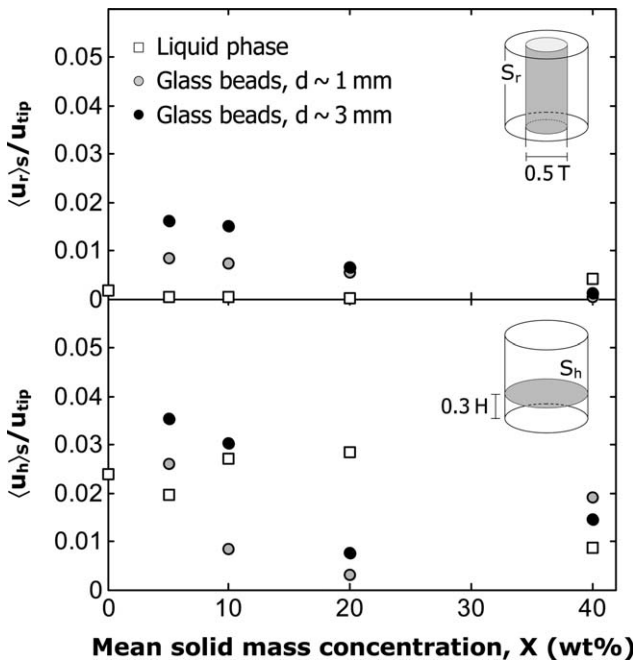

Figure 15. Normalized radial and axial velocities averaged on surfaces S_r (of diameter 0.5T) and S_h (0.3H off the base), respectively.

particle sizes are considerably reduced. Results on spatial phase distribution have showed how local solids build up diminishes for smaller particles and/or higher solids concentrations, with the maximum uniformity index being obtained for the smaller particles at 40 wt % solids. This study has shown that PEPT is a powerful non-intrusive Lagrangian technique, which is ideally suited to the study of dense solid–liquid systems. The technique can, therefore, be extended to the study of more challenging systems with wider particle size distributions, more complex rheologies, and probably even higher concentrations.

Acknowledgments

This research was funded by The Engineering and Physical Sciences Research Council (UK) through Grant GR/S70517/01. We are grateful to Prof. D.J. Parker and Dr X. Fang of the Positron Imaging Center at The University of Birmingham for their assistance with the PEPT experiments.

Notation

C = total mean volume concentration of solids
c_h = mean volume concentration at level h
c_j = local volume concentration of component j
C_j = mean volume concentration of component j
D = impeller diameter (m)
$d\ d_1\ d_2$ = particle diameter (m)
Fl = multi-phase flow number
$Fl^{(j)}$ = flow number of component j
H = height of the suspension (m)
i = cell number
j = mixture component index
k = cylindrical direction index (ϑ, r, or h)
N = impeller rotational speed (s^{-1})
n_c = number of grid cells
n_j = number of particles of component j in the vessel
N_{js} = minimum speed for particle suspension (s^{-1})
O_j = occupancy
$\mathbf{P}$ = tracer location vector (|m|)
Q = total multi-phase impeller pumping rate ($m^3\ s^{-1}$)
$Q^{(j)}$ = impeller pumping rate of component j ($m^3\ s^{-1}$)
$r\ h$ = radial-axial cylindrical coordinates (m)
R = vessel radius (m)
Re_{imp} = impeller Reynolds number (ND^2/v)
S = surface area (m^2)
$S_h\ S_r$ = horizontal planar and vertical cylindrical surface areas (m^2)
s_j = local slip velocity of component j (m s^{-1})
$\overline{s}_j$ = mean slip velocity of component j (m s^{-1})
t = time (s)
T = vessel diameter (m)
t_∞ = PEPT runtime (s)
t_E = Ergodic time (s)
$\mathbf{u}$ = 3D velocity vector (|m s^{-1}|)
$u_\vartheta\ u_r\ u_h$ = cylindrical velocity components (m s^{-1})
u_{rh} = 2D radial-axial velocity magnitude (m s^{-1})
u_{tip} = impeller tip speed (m s^{-1})
V = volume (m^3)
V_j = volume of component j in the vessel (m^3)
V_{Pj} = particle volume of component j (m^3)
V_T = total suspension volume (m^3)
$x\ y\ z$ = Cartesian coordinates (m)
X = total mean mass concentration of solids
$X_1\ X_2$ = mean mass concentration of solid component

Greek letters

ϑ = Azimuthal coordinate (rad)
v = kinematic liquid viscosity ($m^2\ s^{-1}$)
ξ_j = uniformity index of component j
σ_j = standard deviation of normalized c_j

Literature Cited

1. Unadkat H, Rielly CD, Hargrave GK, Nagy ZK. Application of fluorescent PIV and digital image analysis to measure turbulence properties of solid–liquid stirred suspensions. *Chem Eng Res Des*. 2009;87:573–586.
2. Tamburini A, Cipollina A, Micale G, Ciofalo M, Brucato A. Dense solid–liquid off-bottom suspension dynamics: Simulation and experiment. *Chem Eng Res Des*. 2009;87:587–597.
3. Guha D, Ramachandran PA, Dudukovic MP. Flow field of suspended solids in a stirred tank reactor by Lagrangian tracking. *Chem Eng Sci*. 2007;62:6143–6154.
4. Kagoshima M, Mann R. Development of a networks-of-zones fluid mixing model for an unbaffled stirred vessel used for precipitation. *Chem Eng Sci*. 2006;61:2852–2863.
5. Ducci A, Yianneskis M. Turbulence kinetic energy transport processes in the impeller stream of stirred vessels. *Chem Eng Sci*. 2006;61:2780–2790.
6. Chung KHK, Barigou M, Simmons MJH. Reconstruction of 3-D flow field inside miniature stirred vessels using a 2-D PIV technique. *Chem Eng Res Des*. 2007;85:560–567.
7. Chung KHK, Simmons MJH, Barigou M. Angle-resolved Particle Image Velocimetry measurements of flow and turbulence fields in small-scale stirred vessels of different mixer configurations. *Ind Eng Chem Res*. 2009;48:1008–1018.
8. Brunazzi E, Galletti C, Paglianti A, Pintus S. An impedance probe for the measurements of flow characteristics and mixing properties in stirred slurry reactors. *Chem Eng Res Des*. 2004;82:1250–1257.
9. Barresi A, Baldi G. Solid dispersion in an agitated vessel. *Chem Eng Sci*. 1987;42:2949–2956.
10. Wang M, Dorward A, Vlaev D, Mann R. Measurements of gas-liquid mixing in a stirred vessel using electrical resistance tomography (ERT). *Chem Eng J*. 2000;77:93–98.
11. Rammohan AR, Kemoun A, Al-Dahhan MH, Dudukovic MP. A Lagrangian description of flows in stirred tanks via computer-automated radioactive particle tracking (CARPT). *Chem Eng Sci*. 2001;56:2629–2639.
12. Villermaux J. Trajectory Length Distribution (TLD), a novel concept to characterize mixing in flow systems. *Chem Eng Sci*. 1996;51:1939–1946.
13. Wittmer S, Falk L, Pitiot P, Vivier H. Characterization of stirred vessel hydrodynamics by three dimensional trajectography. *Can J Chem Eng*. 1998;76:600–610.
14. Barigou M. Particle tracking in opaque mixing systems: An overview of the capabilities of PET and PEPT. *Chem Eng Res Des*. 2004;82:1258–1267.
15. Doucet J, Bertrand F, Chaouki J. A measure of mixing from Lagrangian tracking and its application to granular and fluid flow systems. *Chem Eng Res Des*. 2008;86:1313–1321.
16. Guida A, Fan X, Parker DJ, Nienow AW, Barigou M. Positron emission particle tracking in a mechanically agitated solid–liquid suspension of coarse particles. *Chem Eng Res Des*. 2009;87:421–429.
17. Barigou M, Chiti F, Pianko-Oprych P, Guida A, Adams L, Fan X, Parker DJ, Nienow AW. Using Positron Emission Particle Tracking (PEPT) to Study Mixing in Stirred Vessels: Validation and Tackling Unsolved Problems in Opaque Systems. *J Chem Eng Jpn*. 2009;42:839–846.
18. Parker DJ, Fan X. Positron emission particle tracking-Application and labelling techniques. *Particuology*. 2008;6:16–23.
19. Fangary YS, Barigou M, Seville JPK, Parker DJ. Fluid trajectories in a stirred vessel of non-newtonian liquid using positron emission particle tracking. *Chem Eng Sci*. 2000;55:5969–5979.
20. Fangary YS, Barigou M, Seville JPK, Parker DJ. A Langrangian study of solids suspension in a stirred vessel by Positron Emission Particle Tracking (PEPT). *Chem Eng Technol*. 2002;25:521–528.
21. Virdung T, Rasmuson A. Measurements of continuous phase velocities in solid–liquid flow at elevated concentrations in a stirred vessel using LDV. *Chem Eng Res Des*. 2007;85:193–200.
22. Altway A, Setyawan H, Margono, Winardi S. Effect of particle size on simulation of three-dimensional solid dispersion in stirred tank. *Chem Eng Res Des* 2001;79:1011–1016.
23. Špidla M, Sinevič V, Jahoda M, Machoň V. Solid particle distribution of moderately concentrated suspensions in a pilot plant stirred vessel. *Chem Eng J*. 2005;113:73–82.
24. Guida A, Nienow AW, Barigou M. PEPT measurements of solid–liquid flow field and spatial phase distribution in concentrated monodisperse stirred suspensions. *Chem Eng Sci*. 2010;65:1905–1914.

25. Fan X, Parker DJ, Smith MD. Enhancing F-18 uptake in a single particle for positron emission particle tracking through modification of solid surface chemistry. *Nucl Instrum Methods Phys Res A*. 2006;558:542–546.
26. Fan X, Parker DJ, Smith MD. Labelling a single particle for positron emission particle tracking using direct activation and ion-exchange techniques. *Nucl Instrum Methods Phys Res A*. 2006; 562:345–350.
27. Parker DJ, Forster RN, Fowles P, Takhar PS. Positron Emission Particle Tracking using the new Birmingham positron camera. *Nucl Instrum Methods Phys Res A*. 2002;477:540–545.
28. Parker DJ, Broadbent CJ, Fowles P, Hawkesworth MR, Mcneil P. Positron Emission Particle Tracking - A technique for studying flow within engineering equipment. *Nucl Instrum Methods Phys Res A*. 1993;326:592–607.
29. Zwietering TN. Suspending of solid particles in liquid by agitators. *Chem Eng Sci*. 1958;8:244–253.
30. Guida A, Nienow AW, Barigou M. Shannon entropy for local and global description of mixing by Lagrangian particle tracking. *Chem Eng Sci*. 2010;65:2865–2883.
31. Atiemo-Obeng VA, Penney RW, Armenante P. Solid–Liquid mixing. In: Paul EL, Atiemo-Obeng VA, Kresta SM, editors. *Handbook of industrial mixing: Science and practice*. Hoboken, NJ: Wiley-Interscience, 2004:543–584.

Manuscript received Apr. 1, 2010, and revision received Sept. 17, 2010.